Treatment of light reflections in 3D PIV systems

OPEN ACCESS
IOP Publishing
Measurement Science and Technology
Meas. Sci. Technol. **36** (2025) 115301 (15pp)
https://doi.org/10.1088/1361-6501/ae1993

Treatment of light reflections in 3D PIV systems

Adrian Grille Guerra*, Laura Porcar Galan, Andrea Sciacchitano and Fulvio Scarano

Delft University of Technology, Faculty of Aerospace Engineering, Delft, The Netherlands

E-mail: a.grilleguerra@tudelft.nl

Received 16 August 2025, revised 10 October 2025
Accepted for publication 30 October 2025
Published 10 November 2025

Abstract

Measuring the velocity field around a complex object by volumetric PIV is hindered by shadow formation (illumination) as well as camera occlusion (imaging). These have been recently dealt with by multiplying illumination and imaging directions (redundancy) and by the integration of ray-tracing techniques to include the effect of visual blockage caused by the object (object-aware particle reconstruction, Wieneke and Rockstroh 2024 *Meas. Sci. Technol.* **35** 055303). The problem of light reflections blinding regions of the images has not been afforded yet. The latter pertains to interactions between illumination and imaging through the object surface and it poses additional challenges to ghost particle formation, particle detection and tracking in general. This study proposes a method to effectively detect such regions, and measures to modify the particle triangulation algorithm. The viability of this novel reflection-aware Lagrangian particle tracking (RA-LPT) approach is examined by application to two experiments of varying complexity. The first case is the flow around a stationary wall-mounted cube as imaged with a redundant number of cameras. The second experiment tackles an elite runner sprinting across the measurement region obtained with the Ring-of-Fire technique. A considerable reduction of ghost particles (false positives) is attained, while the formation of voids (false negatives) is also minimised. The overall result of the method maximises the measurement region around and in proximity of the object of interest.

Keywords: LPT, 3D PTV, STB, reflections, image processing

1. Introduction

While 3D LPT (Schröder and Schanz 2023) represents the state-of-the-art for volumetric velocimetry techniques, the study of the flow around complex objects remains little explored due to inherent limitations of optical access. The literature abounds with experiments conducted in the bulk of flows like for free jets (Violato and Scarano 2011, Huhn *et al* 2018), near and far wakes (Friedhoff *et al* 2021, Scarano *et al* 2022) or wall-bounded flows (Schröder *et al* 2008, Bross *et al* 2023), to mention a few. Exceptions have been achieved using index of refraction matching techniques (Bai and Katz 2014, Schröder *et al* 2020) or traversing and re-orienting the PIV system, for instance employing robotic 3D PIV (Jux *et al* 2018, Schneiders *et al* 2018). For moving targets, such as rotors (Schröder *et al* 2023, Wolf *et al* 2024) or animals (Flammang *et al* 2011, Bomphrey *et al* 2012, Usherwood *et al* 2020) the complexity is further increased, and the measurement domains are most commonly limited to the objects' wakes, after these have left the illuminated/imaged region. Volumetric PIV measurements in the vicinity of objects may enable further understanding of fluid–structure interactions and associated loads (Mertens *et al* 2023), therefore enriching the current capabilities of such systems. An overview of 3D PIV experiments

* Author to whom any correspondence should be addressed.

Table 1. List of volumetric PIV experiments with and without the presence of objects in the measurement domain.

Bulk flow investigations		Object in view	
Research group	Research topic	Research group	Research topic
Flammang *et al* (2011)	Freely swimming fish wake	Jux *et al* (2018)	Full-scale cyclist model, using robotic 3D PIV
Bomphrey *et al* (2012)	Desert locust wakes	Schröder *et al* (2020)	Wall-mounted cube, using refractive index matching
Usherwood *et al* (2020)	Free flying gliding raptor wake	Mertens *et al* (2023)	Flexible wing, moving the 3D PIV system around the object
Friedhoff *et al* (2021)	Ducted propeller wake	Hysa *et al* (2024)	Ship model, partitioning a redundant 3D PIV system
Scarano *et al* (2022)	Cylinder wake	Hendriksen *et al* (2024)	Various static objects, using OA-LPT
Schröder *et al* (2023)	Tip vortex evolution		
Wolf *et al* (2024)	Free flying quadcopter wake		

is listed in table 1, based on the presence of objects in the measurement domain, to provide a comprehensive overview of the state-of-the-art.

The problem of optical blockage has been recently addressed by (Hysa *et al* 2024), who considered both the topics of constrained illumination (shadows) and camera occlusion. Volumetric measurements were conducted around a ship model doubling the illumination direction and with a set of 7 imaging cameras, in excess of the standard 4-camera system used for 3D PIV. In this work, the multiplication imaging paradox became clear: the more cameras are added the more occlusions erode the measurement volume. The proposed solution was partitioning the system into camera sub groups and recombining the results afterwards. An elegant solution to the paradox has been offered by (Wieneke and Rockstroh 2024), who incorporate the object information into the optical model (ray tracing) used for particle detection. With this technique, the formation of camera sub-groups is not necessary and a monolithic system comprises the whole set of cameras. Controlling the object position in the measurement domain is paramount in the above approach and techniques to mark and verify position and shape have been discussed and demonstrated in the study of Hendriksen *et al* (2024) leading to the so-called object-aware Lagrangian particle tracking (OA-LPT). As a result, to date, the problems of shadow formation and optical blockage can be considered as solved.

Another source of optical interference arises from light reflections at the objects' surface. Similar to the previous case of domain erosion due to imaging blockage (Hysa *et al* 2024), light reflections also introduce a paradox: when illumination and imaging directions are multiplied, the regions blinded by excessive illumination progressively erode the measurement domain. In this case, modelling the mechanism producing blinded regions is of formidable complexity as it requires a precise combination of object detection, ray tracing from illumination to imager and modelling reflective/diffusive light-surface interactions.

The problem of light reflections in PIV has been extensively investigated, mostly for planar PIV systems, where the reflection features a bright stripe produced by the laser sheet against the surface. A gamut of best-practice approaches is available from the literature: Kähler *et al* (2006) advise to direct the illumination surface-parallel when possible. When the latter is not possible, Paterna *et al* (2013) propose to treat the object surface with light absorbing paint or employing the principle of fluorescence (Depardon *et al* 2005). Many other studies have focused on image pre-processing in order to separate the light intensity from the particles and that due to background, surface reflections or even ambient light. Adrian and Westerweel (2011) offer a wide discussion of the subject, with most popular choices exploiting the differences between the dot-like particle signal and the broader intensity distribution of the background. Subtraction of pixel minimum intensity in the time domain is also proven an effective method, and Sciacchitano and Scarano (2014) have proposed a frequency domain high-pass filter that eliminates slowly-moving signals from time-resolved image recordings. The use of masking (i.e. total cancellation of the overexposed region) approaches, although robust, is only considered for extreme situations (Masullo and Theunissen 2017), since it involves the loss of velocity information and introduces data gaps.

The specific treatment of light reflections in 3D PIV measurements has barely been discussed in the literature and most recipes are based on the best practice gained from planar PIV. Topologically, the most prominent change is the shift from reflection lines arising from the impingement of a laser sheet on the surface, to more diffuse reflection regions due to the distributed illumination. However, in 3D measurements, regions of high-intensity negatively affect particle triangulation because in the imaging bundle corresponding to the overexposed image the detection algorithms produces a multitude of false positives (a.k.a. ghost particles, Elsinga *et al* 2011), thus locally corrupting the measurement and the particle tracking analysis.

This work aims to provide a generalised procedure for the mitigation of light reflections in volumetric PIV measurements, within the framework of OA-LPT. The work proposes an automated reflection detection method based on the

separation between particles and background signal in the spatio-temporal frequency domain. The method follows with an adaptive masking procedure and involves logics similar to OA-LPT, in this case for the blinded viewing directions. Therefore, regions of the cameras affected by light reflections are treated as optically blocked, such that the particle triangulation and tracking processes are informed accordingly. The article first introduces the mechanism of optical blinding from light reflections, alongside the reflection detection and automated masking procedure. The assessment considers two experimental conditions: the flow around a wall-mounted cube, measured in a wind tunnel; the flow in the wake of a running athlete measured using the Ring-of-Fire (RoF, (Spoelstra *et al* 2019)) apparatus.

2. Background

2.1. Ghost formation in blinded bundles

Volumetric particle tracking algorithms involve both triangulation and tracking steps. In the triangulation process (e.g. iterative particle reconstruction, IPR, (Wieneke 2013), epipolar lines are intersected to find the three-dimensional location of a particle. While in principle two viewing directions are sufficient for triangulation, typically more cameras are employed to reduce the probability of triangulating ghost particles. The region produced by the intersection of all N cameras is denoted as the domain of interest (DOI), where all camera views contribute to the triangulation of particles. Within the DOI, some regions may be covered by $N-M$ cameras only. This circumstance does not necessarily prevent the measurement, as long as the triangulation algorithm is aware of the camera coverage (the region covered by each camera). For the remainder, we recall the concept of camera coverage rank R_c from Hendriksen *et al* (2024) as the integer representing the number of independent views participating the triangulation at each point of the measurement domain. The coverage rank must be at least 2 to enable particle triangulation.

From Elsinga *et al* (2006), a system of N cameras will generate N_g^0 ghost particles in the measurement volume as:

$$N_g^0 = (\text{ppp} \cdot A_p)^N \cdot l_x \cdot l_y \cdot l_z \tag{1}$$

where ppp (particles per pixel) is the particle density in the recordings and A_p is the particle image area. The volume is imaged onto $l_x \cdot l_y$ pixels and l_z represents the depth in voxel units.

Let us assume that in a region of the object surface in the DOI light is scattered towards the imagers, as illustrated in figure 1 (left) for a system of $N = 3$ cameras. A portion of the sensor A_r^i, with the superscript i indicating the camera index, in each of the three cameras will receive light from the particle tracers superimposed to the direct scattering/reflection from the surface referred to as blinded areas. In this context, the term blinding is intended as the condition of a significantly increased light intensity compared to the remaining of the image. Such intensity does not necessarily need to exceed the saturation level to blind the view. The blinded viewing directions (i.e. blinded bundle $A_r^1 \cdot l_z$) from camera 1 is prone to produce ghost particles (G), at any intersection of epipolar lines from cameras 2 and 3. The equation proposed by Elsinga et al (2006) is modified here for the purpose of estimating the number of ghost particles produced inside a blinded bundle, N_g^1, which reads as:

$$N_g^1 = (\text{ppp} \cdot A_p)^{N-1} \cdot A_r^1 \cdot l_z \tag{2}$$

with the lower exponent ($N-1$ instead of N) suggesting that N_g^1 will quickly exceed N_g^0.

The problem of ghost formation is exacerbated in the regions where blinded bundles intersect. For instance, in the intersection between cameras 1 and 2 ($(A_r^1 \cdot l_z \cap_{r^2}^{A} \cdot l_z)$), $N_g^{1,2}$ ghost particles will be formed, as:

$$N_g^{1,2} = (\text{ppp} \cdot A_p)^{N-2} \cdot \left(A_r^1 \cdot l_z \cap A_r^2 \cdot l_z\right). \tag{3}$$

A generalised formulation for a N-camera system yields an estimate of N_g ghost following the equation below:

$$\begin{aligned} N_g = N_g^0 + \sum_{i=1}^{N} N_g^i + \sum_{i=1}^{N-1}\sum_{j=i+1}^{N} N_g^{i,j} + \cdots + N_g^{1,\cdots,N} = \\ = (\text{ppp} \cdot A_p)^N \cdot l_x \cdot l_y \cdot l_z + \sum_{i=1}^{N} (\text{ppp} \cdot A_p)^{N-1} \cdot A_r^i \cdot l_z \\ + \sum_{i=1}^{N-1}\sum_{j=i+1}^{N} (\text{ppp} \cdot A_p)^{N-2} \cdot \left(A_r^i \cdot l_z \cap A_r^j \cdot l_z\right) + \cdots \\ + \left(A_r^1 \cdot l_z \cap A_r^2 \cdot l_z \cap \cdots \cap A_r^N \cdot l_z\right). \end{aligned} \tag{4}$$

The ratio between ghost and actual particles is often taken as a measure of reconstruction accuracy. Equations (1) and (4) are evaluated below under typical conditions of seeding density ppp = [0.001–0.02], particle diameter $d_\tau = 2$ px and fraction of area affected by light reflections $A_r^* = [0–0.1]$. Furthermore, the evaluation considers a varying number of cameras N.

An accurate particle field reconstruction is characterised by $\frac{N_g}{N_p} < 0.1$. Figure 2 (left) indicates that in absence of reflections, a system of four cameras is sufficient to reconstruct faithfully a particle field at ppp = 0.01. To incorporate light reflections into the discussion, a simplified situation is considered. It is assumed that reflections affect all cameras equally, and that the imagers observe the DOI with a constant angular separation between them (tomographic aperture angle, θ) of $\theta = \pi/4$, such that the intersection bundle of k cameras can be simply estimated as:

$$A_r^1 \cdot l_z \cap A_r^2 \cdot l_z \cap \cdots \cap A_r^k \cdot l_z = \frac{(A_r)^{3/2}}{2^{k-1}\tan\theta}. \tag{5}$$

For such conditions, the ratio N_g/N_p is given in figure 2 (right). Overall, a reduction in the particle reconstruction

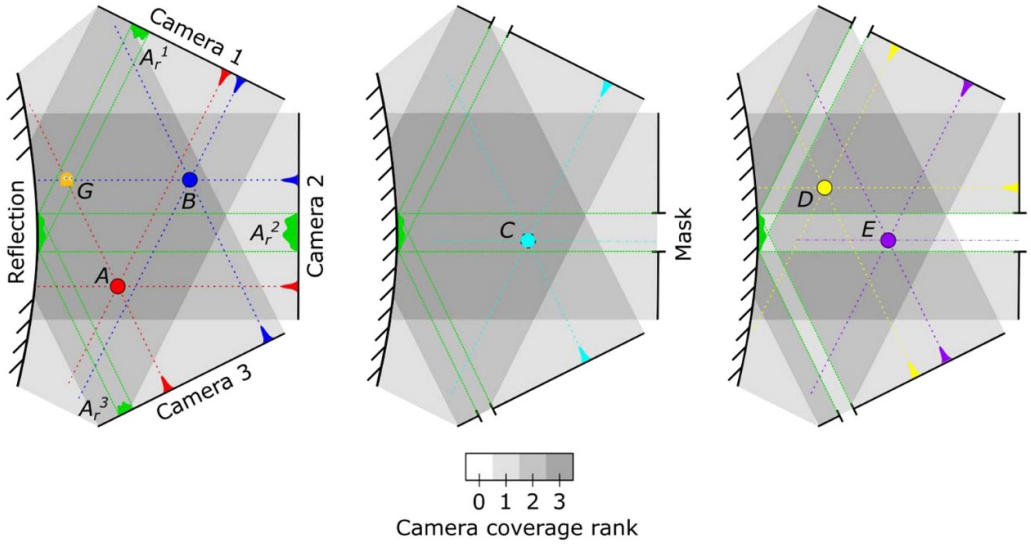

Figure 1. Camera coverage rank R_c and particle triangulation for a 3-camera system in presence of a finite region of light reflection. Left: two particles (A) and (B) are triangulated and a ghost (G) is formed in the blinded bundle of camera 1. Middle: blinded bundles are masked (value set to zero). A single particle (C) is triangulated by cameras 1 and 3 and falls within the masked region of camera 2, hence it is not reconstructed. Right: the blinded bundles are excluded by the triangulation process (object aware) and the two particles (D) and (E) are reconstructed even when one (E) falls inside a single blinded bundle.

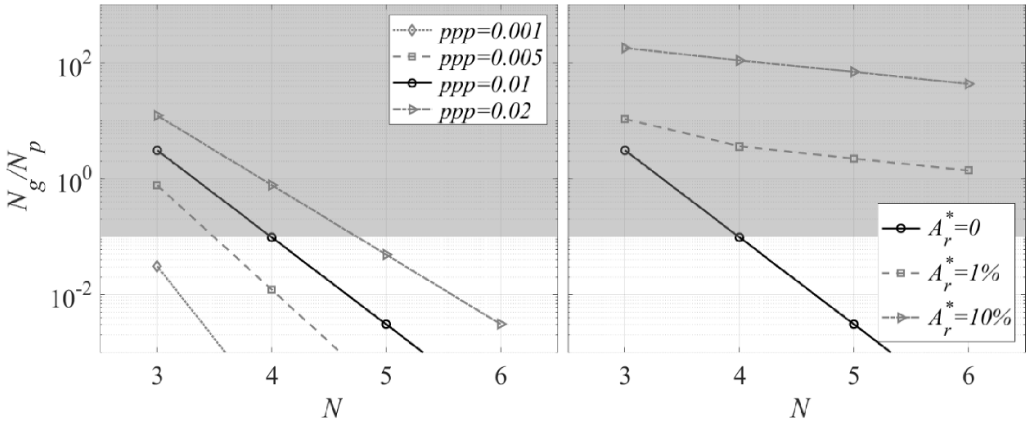

Figure 2. Ratio of ghost to real particles (N_g/N_p) as a function of the number of cameras N. Left: in the absence of light reflections, for varying *ppp* levels (equation (1). Right: for images affected by light reflections (equation (4)), for varying reflection areas and ppp = 0.01. Acceptable range is considered below 0.1 ($N_g/N_p < 10\%$) and the region above such level is shaded to indicate conditions of overly corrupted reconstruction.

quality is observed. More importantly, increasing the number of cameras is a less effective measure to reduce spurious triangulations. Therefore, for an experiment affected by blinded bundles, adding new cameras does not provide further information, and ghost particles will still be formed in the affected areas.

2.2. Deactivation of blinded bundles

A possible solution to the problem of ghost formation modelled by equation (4) is that the regions of the measurement domain that correspond to the reflections (blinded bundles) are excluded from the process of particle image triangulation. As a consequence, the coverage rank decrease in blinded bundle and the triangulation makes use of the remaining, not blinded, views. Bundle deactivation is a procedure similar to that devised by Wieneke and Rockstroh (2024) to deactivate regions of the DOI obscured by the object presence. In that case, the position of the delimiting surface requires knowledge of the object position. Instead, for a blinded bundle, such information is not needed being the bundle deactivated along its entire depth. However, the identification of such bundle requires identification of the blinded area A_r on the sensor, in turn opening the problem of reflection detection.

Sample views from the 3D measurements around a scaled cyclist from Hendriksen *et al* (2024), shown in figure 3, render the complexity of imaging the seeding tracers in the regime of volumetric illumination and imaging. The recording features regions where the tracers are clearly distinct from the background. In other regions, some background light is visible

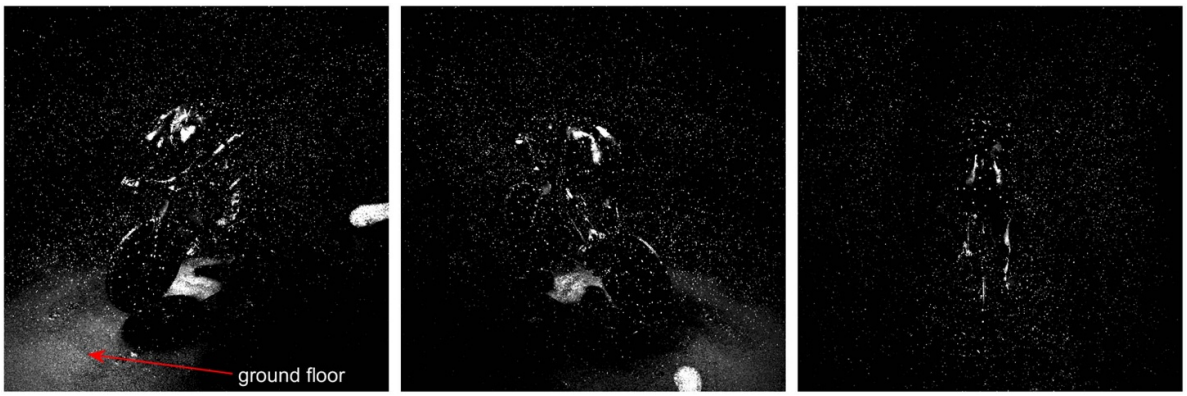

Figure 3. Raw PIV images as seen from three cameras from measurements around a scaled cyclist (Hendriksen *et al* 2024), including the presence of light reflections emanating from the object's surface.

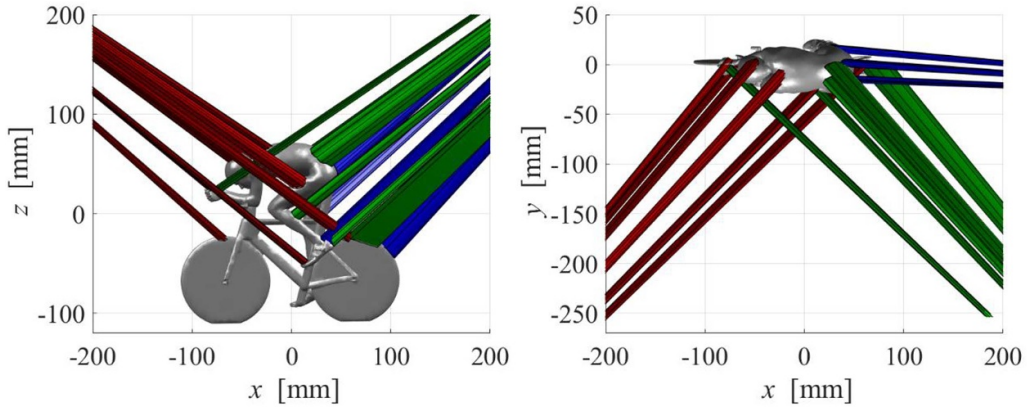

Figure 4. Side (left) and top (right) view of the blinded bundles affecting three cameras from the experiments of Hendriksen *et al* (2024) on the flow around a scaled cyclist.

(e.g. ground floor, see the annotation in figure 3 (left)) and it can be often removed by time-average or time-minimum intensity subtraction. Finally, some bright regions emanate from the points where the light impinging onto the surface is reflected directly towards the imager. Such regions often feature a high intensity, and the image corruption is not recoverable by a simple subtraction. These regions are therefore considered as 'blinded' and their back projection in three-dimensional space are the blinded bundles. An example of such blinded bundles for the images given in figure 3 are illustrated in figure 4. The blinded bundles from the three camera views shown in figure 3 left, middle and right are indicated in red, green and blue respectively. The complexity of the geometry causes the appearance of multiple blinded bundles, with some of them intersecting in small regions of the DOI.

A straightforward approach for blinded bundle deactivation consists in setting the intensity level to zero within A_r (figure 1-middle), provided such area has been detected. However, the shortcoming of such approach is that all particles in the blinded bundle will be neglected (C), leading to significant gaps in the measurement domain. Recalling the nomenclature introduced by (Hysa *et al* 2024), a volumetric loss V_{loss} of the DOI is formed, considering the union of the blinded bundles as:

$$V_{\text{loss}} = \text{DOI} \cap (A_r^1 \cdot l_z \cup A_r^2 \cdot l_z \cup \cdots \cup A_r^N \cdot l_z). \tag{6}$$

The above corresponds to the condition that a particle can be reconstructed if and only if it is triangulated by all the available N viewing directions. It can be easily demonstrated that by the above approach, further adding cameras paradoxically leads to an increased volumetric loss of the measurement.

A less invasive solution is that of masking (viz. disabling) the reflected regions, while adopting the (OA-LPT, Wieneke and Rockstroh 2024) to the blinded bundles. In the reflection-aware context (RA-LPT), the requirement for particle reconstruction is relaxed to triangulation from a subset of $N-M$ cameras (in this context $N-M$ corresponds to the camera rank R_c), which does not include the M cameras blinded at the specific location of reconstruction. By the latter approach (figure 1-right), the formation of ghost particles can be mitigated and the measurement domain erosion only includes the regions where more than $N-2$ blinded bundles intersect. In this example, particles can be reconstructed in regions unaffected by reflections (D) and also inside single blinded bundles (E).

Figure 5 exemplifies the above discussion by illustrating the distribution of coverage rank based on the principle of blinded bundles intersection (equation (5)). The example consists of

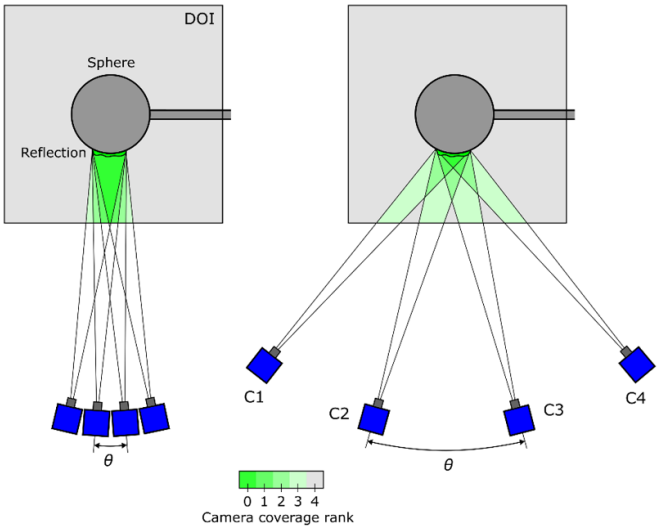

Figure 5. Camera coverage rank for a 4-camera system looking at a sphere under volumetric illumination. Left: for a low tomographic aperture system ($\theta = 4°$). Right: for a higher tomographic aperture ($\theta = 30°$).

four cameras observing a sphere, representative of the measurements from Jux *et al* (2020). In the original experiments, the use of a coaxial volumetric velocimeter (CVV, Schneiders *et al* 2018) for illumination and imaging produced the situation illustrated in figure 5 (left), where the blinded bundles intersect over a relatively large volume. Considering a minimum coverage rank of $R_{\min} = 3$ for particle triangulation (instead of the default 2), a loss of approximately $V_{\text{loss}} = 6\%$ of the DOI is formed. The scenario is improved employing a more conventional camera arrangement with higher tomographic aperture, of $\theta = 30°$, as illustrated in figure 5 (right), where $V_{\text{loss}} = 3\%$ of the DOI and the missing region is kept closer to the object surface.

2.3. Reflection identification and masking

From the above it is clear that any method that requires blinded bundle deactivation requires knowledge of the blinded region in the domain, in turn asking for identification of the image region overexposed by light reflections. Volumetric PIV light reflections tend to be more diffuse compared to the typical bright stripe encountered in planar PIV. Often such reflections do not saturate the sensor, however their shape and intensity can largely vary which complexifies their identification.

A raw image from the volumetric PIV experiment around a sphere of Jux *et al* (2020) is shown in figure 6 (left). Particle images appear as tiny dots; the sphere surface is not visible, but indicated by a dashed green line; the region of reflection is a rather circular blob with maximum intensity at the middle and decaying radially.

In this example, the reflection is stationary, and therefore image pre-processing by subtracting the (sliding) time-minimum along the recording sequence is a proven approach (Gui *et al* 1997). The result is shown in figure 6 (middle), where the reflection intensity is attenuated. Yet some time variations due to model-camera vibrations and illumination jitter prevent full elimination of the reflected light. A spatial high-pass filter (Willert 1997) yields similar results (figure 6-right). In general, separating particles image intensity from the background remains a challenging problem lacking a universal solution. The problem becomes particularly intricate when dealing with reflections that vary in space and time. In this respect, image masking is considered a more viable approach.

Here, we consider the reduction of the reflection intensity level associated with the image pre-processing methods as shown in figure 6; by a comparison with the raw image, the region of largest disparity can be identified to form a processing mask (Porcar Galan *et al* 2024). While any method available in the literature could be used for this purpose, the approach discussed here aims at generalising the procedure such to be suited for both stationary as well as fast-moving reflections.

The method combines time-based and spatial-based filters. In the time domain, a third-order Butterworth high-pass filter is considered (Sciacchitano and Scarano 2014), that tackles the contribution of stationary or slow-moving reflections. The filter is defined by the cut-off frequency f, expressed in terms of the Nyquist acquisition frequency. In the spatial domain, a high-pass filter with a Gaussian isotropic kernel is considered, to tackle reflection areas bigger than the particle images. When implemented in the frequency domain (Porcar Galan *et al* 2024), the filter is defined by a cut-off wavenumber κ. The resulting operator can be considered acting in the frequency–wavenumber space as a high-pass filter. In the remainder, the combined method will be referred to as spatio-temporal high-pass filter. For computational efficiency both approaches are implemented in the frequency domain, as can be found in the script given as supplementary material of the article (Grille Guerra *et al* 2025). Applying this methodology, with $f = 0.1$ and $\kappa = 0.01$ 1/px (please refer to Sciacchitano and Scarano 2014, Porcar Galan *et al* 2024 for the choice of appropriate spatio-temporal cut-offs respectively) to the raw image in figure 6 (left) returns the image shown in figure 7 (left). Due to the combination of time and space information, the analysis outperforms that of previously discussed methods, but still fails to fully separate the particle images from the background for its complete elimination.

Therefore, the approach aims at a producing a mask from the normalised comparison between raw (i) and pre-processed (j) images. The operation follows the concept of the structural similarity index measure (SSIM,) introduced by Wang *et al* (2004), which reads as:

$$\text{SSIM}\,(i,j) = \frac{(2\mu_i\mu_j + c_1)\,(2\sigma_{ij} + c_2)}{\left(\mu_i^2 + \mu_j^2 + c_1\right)\left(\sigma_i^2 + \sigma_j^2 + c_2\right)}, \qquad (7)$$

where μ_i, μ_j, σ_i, σ_j and σ_{ij} are the local (over a Gaussian window) mean, standard deviation and covariance of the images, and c_1 and c_2 are small regularisation constants. This metric is frequently adopted in machine vision to assess the quality of image compression. The operator yields unity for identical images, and tends to zero when changes in intensity and contrast are significant. The SSIM between the raw image in

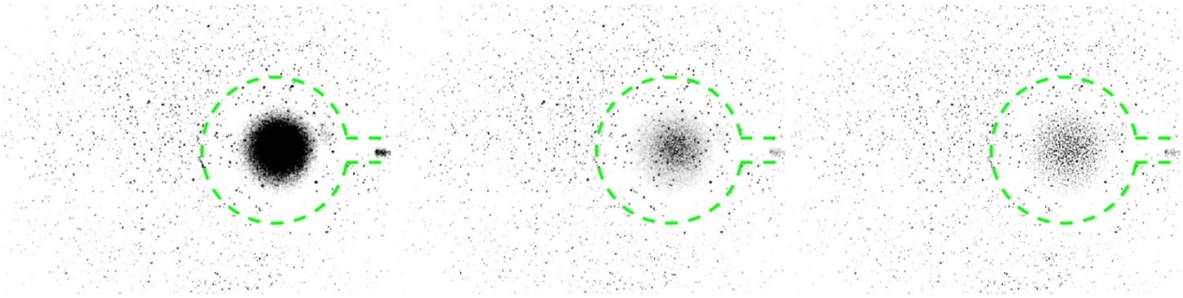

Figure 6. Images of the flow around a sphere (inverted greyscale), indicated by the green dashed line, obtained from a 3D PIV system. Left: raw image. Middle: pre-processed image after subtraction of the minimum intensity in time. Right: pre-processed image obtained via high-pass filtering in space.

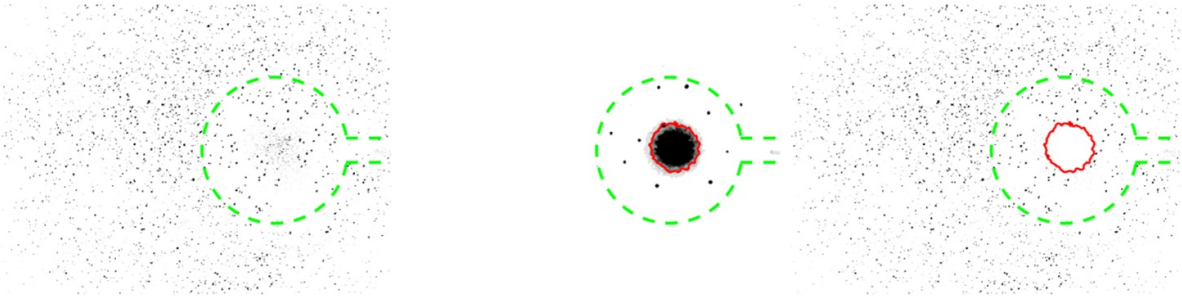

Figure 7. Image pre-processing approach applied to an image of the flow around a sphere, indicated by the green dashed line, obtained from a 3D PIV system. Left: image pre-processed via spatio-temporal high-pass filtering. Middle: SSIM between raw and pre-processed images, with SSIM $= 0.5$ indicated by a red line; dark indicates low values of SSIM, whereas white represents SSIM $= 1$. Right: masking applied to the pre-processed image for SSIM < 0.5.

figure 6 (left) and the pre-processed image in figure 7 (left) is illustrated in figure 7 (middle). Lower values in the reflection area can be used as indicator of reflection. A few dots are visible too, due to the object markers painted on the surface of the sphere. A reflection detection criterion is chosen as SSIM $<$ 0.5, which is indicated in figure 7 (middle) by a red line. The region inside this boundary is then considered blinded and the corresponding blinded bundle is evaluated by ray tracing and deactivated from the process of particles reconstruction. Masking this region in the pre-processed image finally returns the image shown in figure 7 (right), where the blinded region intensity level is set to zero for readability.

The computational cost of the additional masking step is comparable to that of the pre-processing stages. For the images of the test case presented in section 3.1 (100 snapshots and 10 cameras in double-frame mode), the involved CPU times for the Butterworth temporal high-pass filter, the spatial high-pass filter and the masking step were approximately 300 s, 100 s and 150 s respectively, with all methods implemented on *Matlab 2024b* running on an *Intel(R) Xeon(R) W-2223* processor. This means that the image masking added an extra 37.5% of computational time.

3. Experimental assessment

Two experiments are presented that demonstrate the viability and the performance of the method. The first is conducted in a low-speed wind tunnel facility, and consists of measurements around a wall-mounted cube (Hendriksen *et al* 2025). The region of interest is illuminated from four different directions, and the particles are imaged from ten directions. The low acquisition frequency of the cameras limits the measurements to double-frame mode, and the particle tracking is done using the so-called two-pulse Shake-the-Box algorithm (Novara *et al* 2023).

In the second experiment, the velocity field around and past a running athlete (D'Angelo *et al* 2025) is measured using the RoF system (Spoelstra *et al* 2019). Light is provided from a single illumination direction in form of a 30 cm thick slab. The light scattered by the tracers is collected with only three high-speed cameras and time-resolved particle tracking makes use of the Shake-the-Box algorithm (Schanz *et al* 2016). The athlete crossing the illuminated region produces strong and fast-varying reflection regions in all cameras.

Both experiments make use of sub-millimetre helium-filled soap bubbles (Scarano *et al* 2015) as tracers, resulting in good image quality thanks to their excellent light scattering characteristics. The most relevant experimental parameters are summarised in table 2.

3.1. Wall-mounted cube

The flow around a wall-mounted cube with a side length of 10 cm is measured in the W-Tunnel of the Faculty of Aerospace Engineering of TU Delft, an open jet facility with a cross section of 60×60 cm^2. The cube is mounted at zero incidence, i.e. its faces are parallel and perpendicular to the

Table 2. Measurement parameters of the two experiments.

	Wall-mounted cube (wind tunnel)	Running athlete (Ring-of-Fire)
Tracer particles	HFSB	HFSB
Illumination	4 x *LED Flashlight 300* (300 W)	4 x *LED Flashlight 300* (300 W)
Imaging	10 x LaVision *Imager LX* (CCD, 2 MPx, 4.4 μm pitch, 14 bit)	3 x Photron *Mini AX100* (CMOS, 1 MPx, 20 μm pitch, 12 bit)
Reference velocity (m s^{-1})	10 (free stream)	8 (running speed)
Measurement volume (L)	125	2200
Acquisition frequency (Hz)	8 (double-frame)	400
Pulse duration (μs)	25	250
Pulse separation (μs)	250	2500
Objective focal length (mm)	25	50
Digital image resolution (px mm^{-1})	4.4	0.4
f-number $f_\#$	8	5.6
Particles per pixel (ppp)	0.01	0.03

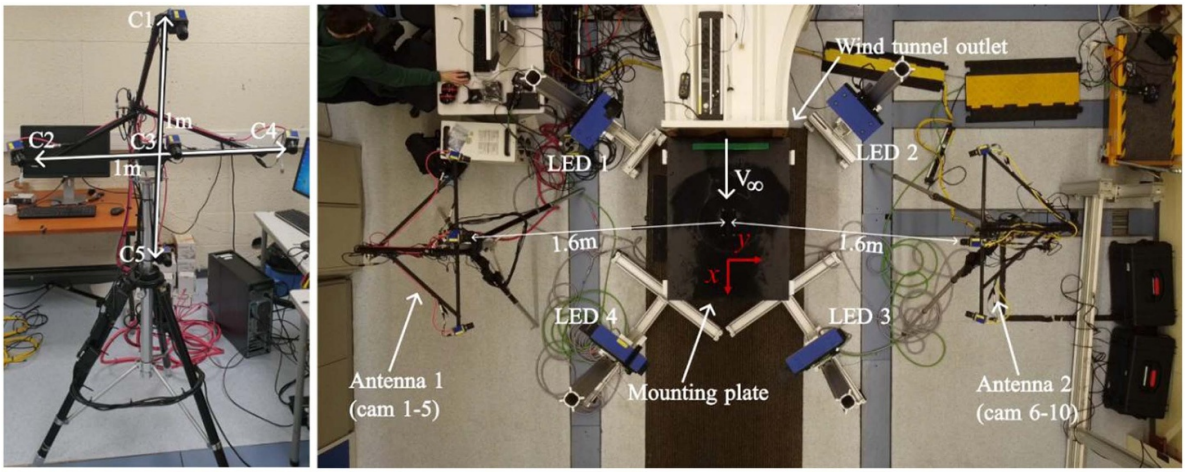

Figure 8. Experimental setup of the wind tunnel measurements of the flow around a wall-mounted cube. Left: arrangement of five cameras in an antenna array. Right: top-view of the setup, containing the wind tunnel outlet, illumination, imaging and mounting plate for the object of interest.

freestream direction. The freestream speed is set to $U_\infty = 10$ m s^{-1} ($Re = 70,000$). The flow is seeded with neutrally-buoyant HFSB, released by an in-house 200-generator seeding rake installed in the settling chamber of the wind tunnel (Saiz *et al* 2022). To avoid optical blockage due to shadow regions, a measurement volume of approximately $50\times50\times50$ cm^3 is illuminated from various directions using four LaVision *LED-Flashlight 300* modules. Similarly, a total of ten LaVision *Imager LX* cameras (2 MPx, 4.4 μm pitch, 14 bit) are placed around the object to compensate for optical blockage due to camera occlusions. The cameras are mounted on two arrays, containing five cameras each, referred to as *antennas*. The camera arrangement of such antennas is shown in figure 8 (left). The cameras are equipped with 25 mm focal length objectives and the f-number is set to $f_\# = 8$ in order to achieve the desired depth of field. For the given configuration, this results in a digital image resolution of 4.4 px mm^{-1}. A top-view of the experimental setup is given in figure 8 (right).

The maximum acquisition frequency of the chosen cameras is insufficient for time-resolved particle tracking, and thus the measurements are conducted in double-frame mode, at a frequency of 8 Hz, and velocity information is obtained via TP-STB. To maximise illumination, the LED modules are operated in overdrive mode, using a pulse width of 25 μs, which results in a pulse energy of 7.25 mJ. The pulse separation is therefore set to 250 μs, respecting the duty cycle of the hardware, which corresponds to a typical particle displacement of around 10 px in the images.

Each antenna is calibrated independently using a planar calibration plate that is shifted and rotated in the measurement volume, and the two arrays are coupled together using a wand-based approach (Nutta *et al* 2023). A pinhole camera model is considered, and refined based on a volume self-calibration (Wieneke 2008) performed on the particle images. Calibration, particle tracking and data postprocessing operations are performed in the DaVis 11.2 software, which incorporates OA capabilities (Wieneke and Rockstroh 2024).

The relative location of illumination and imaging within the experimental setup causes the appearance of light reflection regions in some cameras. For instance, camera 1 (top camera in antenna 1, see figure 8) is mostly unaffected, as shown in figure 9 (left). While the location of the cube can be recognised

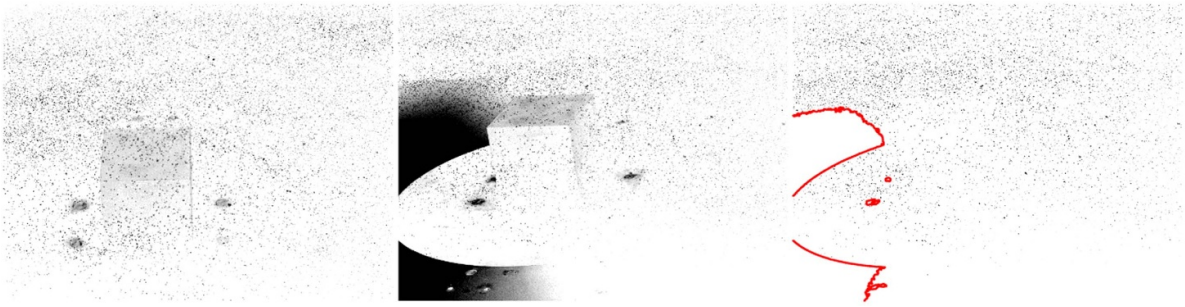

Figure 9. Experimental images of the flow around a wall-mounted cube. Left: raw image in camera 1, looking at the cube from above. Middle: raw image from camera 2, looking at the cube from downstream. Right: pre-processed image (spatio-temporal high-pass filter) from camera 2, with generated mask indicated by red lines.

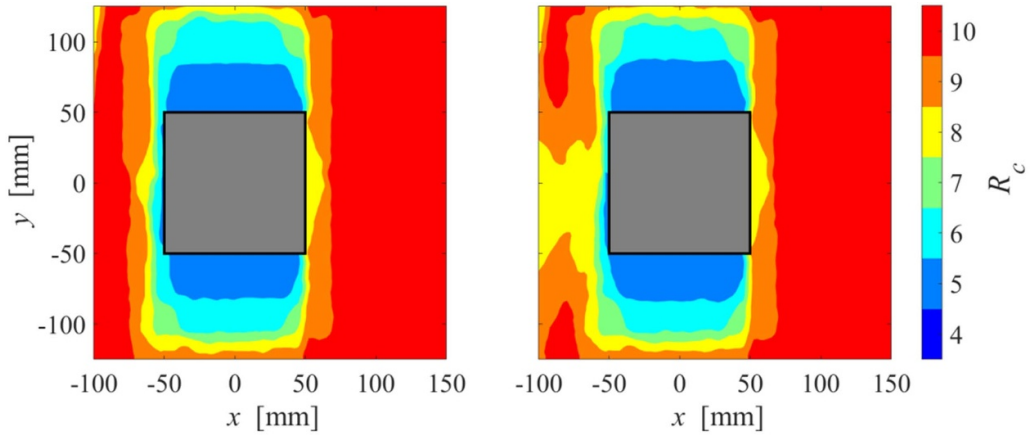

Figure 10. Camera coverage rank R_c around the cube in a slice at a height of $z = 75$ mm from the wall. Left: where only optical blockage due to camera occlusion has been considered. Right: where both camera occlusion and light reflection have been considered.

in the raw image, the pixel intensity in this area is weaker than that of the particle images and it can be filtered out effectively. Instead, camera 2 (downstream camera in antenna 1) is affected by the position of the upstream illuminator on the opposite side of the cube, whose light reflects from the mounting plate corrupting part of the image, as shown in figure 9 (middle). Using the automated masking approach discussed in section 2.2, with $f = 0.1$ and $\kappa = 0.01$ 1/px, transforms the image into the one shown in figure 9 (right). The pre-processed image contains a mask in the light reflection region coming from the mounting plate and two smaller masks at the mounting points of the cube, indicated by red lines in the figure.

The spatial location of the generated masks can be incorporated into the OA-LPT framework as another source of optical blockage. Without it, all contributions in the present experiment arise from camera occlusions due to the presence of the cube in the measurement domain. This is illustrated in figure 10 (left), by showing a slice of the camera coverage rank R_c at a height of $z = 75$ mm from the mounting plate. R_c is extracted directly from the TP-STB analysis, by reducing the particle-based results onto a Cartesian grid using an ensemble-averaging approach, collecting samples from 100 snapshots and averaging over bins with a side length of 1 cm and 75% overlap. In the wake of the cube, all ten cameras have optical access, while this number reduces closer to the object, with only five cameras seeing each side of the cube close to the surface.

Including the optical blockage arising from the presence of light reflections in the downstream imagers results in the coverage rank shown in figure 10 (right). At this height, the reflections coming from the mounting plate have an effect on the front part of the cube, with the rank reducing from ten to eight due to two cameras being affected.

The impact of the masking approach and the inclusion of masks in the OA-LPT framework is discussed in the following, both in terms of the particle tracking analysis and Cartesian grid reduction results. A benchmark is established employing images that have been pre-processed using the approach introduced in section 2.2, but without the masking step, so that reflections are attenuated and not removed completely. This represents a typical scenario of image pre-processing for volumetric PIV, and resembles the situation sketched in figure 1 (left). Particle tracks extracted from the TP-STB analysis are shown in figure 11 (left), coloured by streamwise velocity. For improved visualisation, only a small region around the cube is included, and up to a height of $z = 100$ mm from the wall, from an ensemble of 5 snapshots. Notably, the remaining intensity in the regions of reflection causes the appearance of an agglomeration of ghost particles at the mounting points of the cube ($z = 0$), indicated by purple circles in the figure.

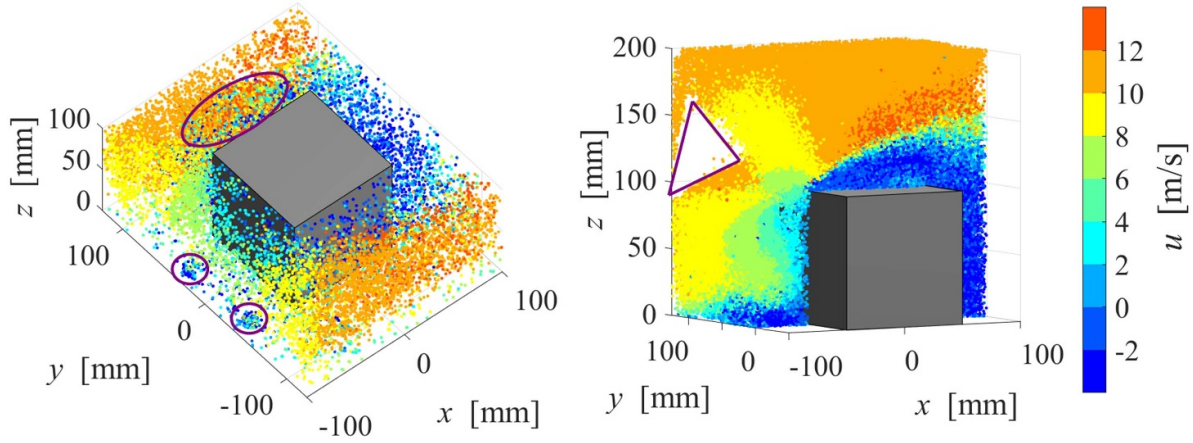

Figure 11. Particle tracks in the surroundings of the wall-mounted cube, coloured by streamwise velocity. Left: images have been pre-processed with the spatio-temporal high-pass filter but not masked, and regions dominated by ghost particles are indicated in purple. Right: images have been masked, but optical blockage has not been accounted for. Region void of particles indicated in purple.

These locations can be already observed in the raw images, as for example the one shown in figure 9 (middle). Besides, ghost particles are triangulated in regions where fewer cameras have optical access, this is, close to the sides (see figure 10 (left)). The region next to the lateral face at positive y is particularly clear, with particles of high velocity being tracked in a region where flow separation is expected. The asymmetric behaviour between the two sides of the cube is attributed to a slightly different location and orientation of the LED illuminators, which produced a more severe reflection in the positive y side. This behaviour is in line with the discussion introduced in section 2.1, as reflections cause the appearance of ghost particles (false positives) throughout the domain.

The appearance of ghost particles can be attenuated by masking the regions affected by light reflections, as sketched in figure 1 (middle). Without further modifications to the particle tracking algorithm, this solution introduces the problematic of false negatives (regions void of particles), since particles travelling over masked areas cannot be found in all cameras that have optical access. The situation is illustrated in figure 11 (right), which shows particle tracks extracted from masked images (see figure 9 (right)), while requiring R_c to follow the behaviour given in figure 10 (left). For visualisation purposes, only a region for $y > 0$ is included in the figure, from an ensemble of 100 snapshots. The results show the appearance of a bundle void of particles in the domain, indicated in purple, which belongs to the propagation of a mask along the line of sight of the affected camera. The comparison between the two situations given in figure 11 reveals that, without image masking, the ratio of ghost to real particles is approximately $N_g/N_p = 0.35$. On the other hand, a volumetric loss of $V_{loss} = 8\%$ of the DOI is introduced by masking the reflection areas.

Both situations (false positives and false negatives) affect the time-averaged velocity field once reduced onto a Cartesian grid (using the same ensemble-averaging parameters as discussed earlier for R_c). Contours of the time-averaged streamwise velocity and the standard deviation of streamwise velocity, extracted at a slice at a height of $z = 75$ mm from the wall are shown in figure 12 (top) and figure 12 (bottom) respectively. The results shown in figure 12 (left) are obtained without the masking step. Here, ghost particles corrupt the solution close to the surface on the sides, as anticipated in figure 11 (left). This behaviour is more noticeable for $y > 0$, where no flow separation can be observed and high velocity fluctuations are measured in potential flow areas upstream and to the side of the cube.

The solution shown in figure 12 (middle) is the one obtained when masking the images but not modifying the required R_c, extracted from the particle tracks shown in figure 11 (right). This case is affected by false negatives, and no time-averaged solution can be obtained in a region upstream of the cube. Both false positives and false negatives can be avoided employing the approach introduced in this article, resembling the situation sketched in figure 1 (right). Masking the images and modifying the required camera coverage rank to match the one shown in figure 10 (right) returns the velocity field shown in figure 12 (right). This solution does not contain any data gaps and no significant effect of ghost particles can be appreciated. The flow field agrees well with results in the literature (Schröder *et al* 2020), including flow separation on the sides and a recirculation region in the wake extending more than a side length downstream of the back face.

3.2. Running athlete

The flow field around a running athlete has been measured experimentally in an indoor sprint hall at the Omnisport sport facility, located in Apeldoorn, The Netherlands. Prior to the experiments, the participant signed an informed consent form. The approximate running speed is 8 m s^{-1} ($Re \sim 200\,000$ based on a shoulder width of 0.4 m), measured using a laser Doppler device (Jenoptik *Laveg LDM 300 C*, (Ashton and Jones 2019)). The flow is seeded using HFSB, generated by the same seeding rake discussed earlier for the wall-mounted

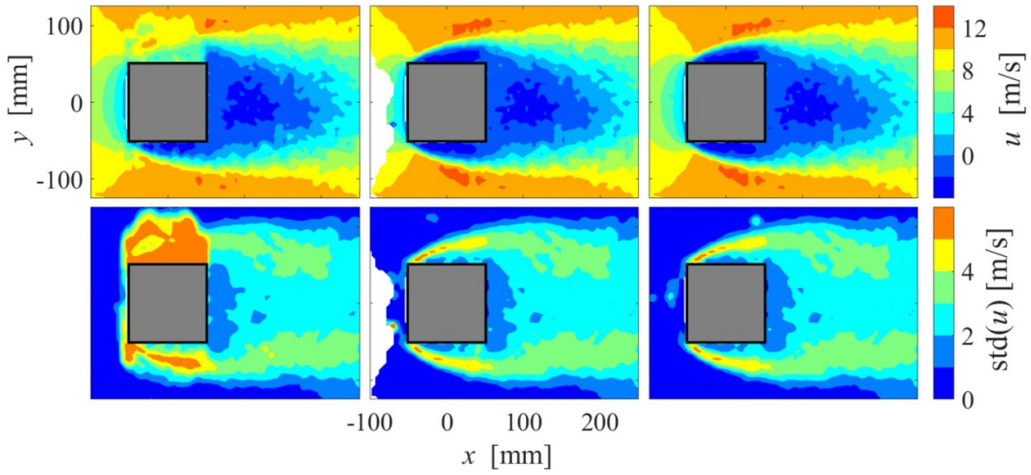

Figure 12. Contours of time-averaged streamwise velocity (top) and standard deviation of streamwise velocity (bottom) at a height of $z = 75$ mm from the wall. Left: images have been pre-processed with the spatio-temporal high-pass filter but not masked. Middle: images have been masked, but optical blockage has not been accounted for. Right: images have been masked and optical blockage has been accounted for.

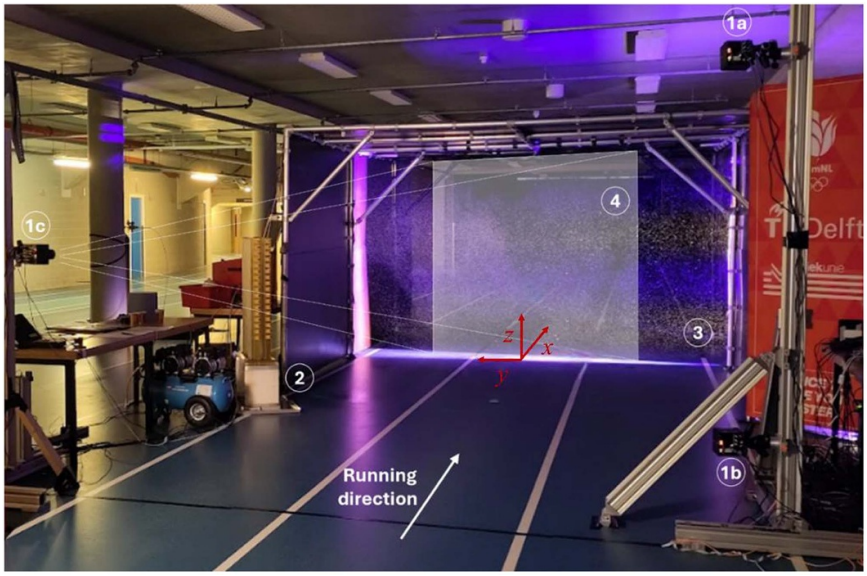

Figure 13. Picture of the experimental arrangement of the on-site measurements of the flow in the wake of a running athlete. High-speed cameras (1), seeding rake (2), LED modules (3) and region of interest (4).

cube experiment. A region of $0.3 \times 2.7 \times 2.7$ m^3 ($x\,x\,y\,x\,z$) is illuminated using four LaVision *LED-Flashlight 300* modules, and imaged using three Photron *Mini AX100* high-speed cameras (CMOS, 1 MPx, 2 μm pitch, 12 bit) equipped with 50 mm focal length objectives set to $f_{\#} = 5.6$. For the chosen configuration, the resulting digital image resolution is equal to 0.4 px mm^{-1}. A picture of the experimental setup is given in figure 13.

The recording sequence, triggered by a photoelectric sensor, consists of a series of 1000 images acquired at 400 Hz, using an illumination pulse duration of 250 μs (pulse energy of 72.5 mJ). This results in a covered distance of approximately 20 m, of which 14 m correspond to the athlete's wake. Camera calibration is performed using a custom two-level calibration plate, employing a pinhole camera model later refined via VSC (Wieneke 2008) from the particle images.

The present analysis focuses on the near wake of the athlete. While passing through the illuminated region, light reflects from the skin and clothing causing the appearance of a strong reflection in the cameras. This changes rapidly from frame to frame posing additional challenges to the image pre-processing stage. Raw and pre-processed images are shown in figure 14 (top) and figure 14 (bottom) respectively, for a frame when the athlete has almost made it through the illuminated slab. The images have been dewarped to the plane $x = 0$ for a better representation of the perspective angle.

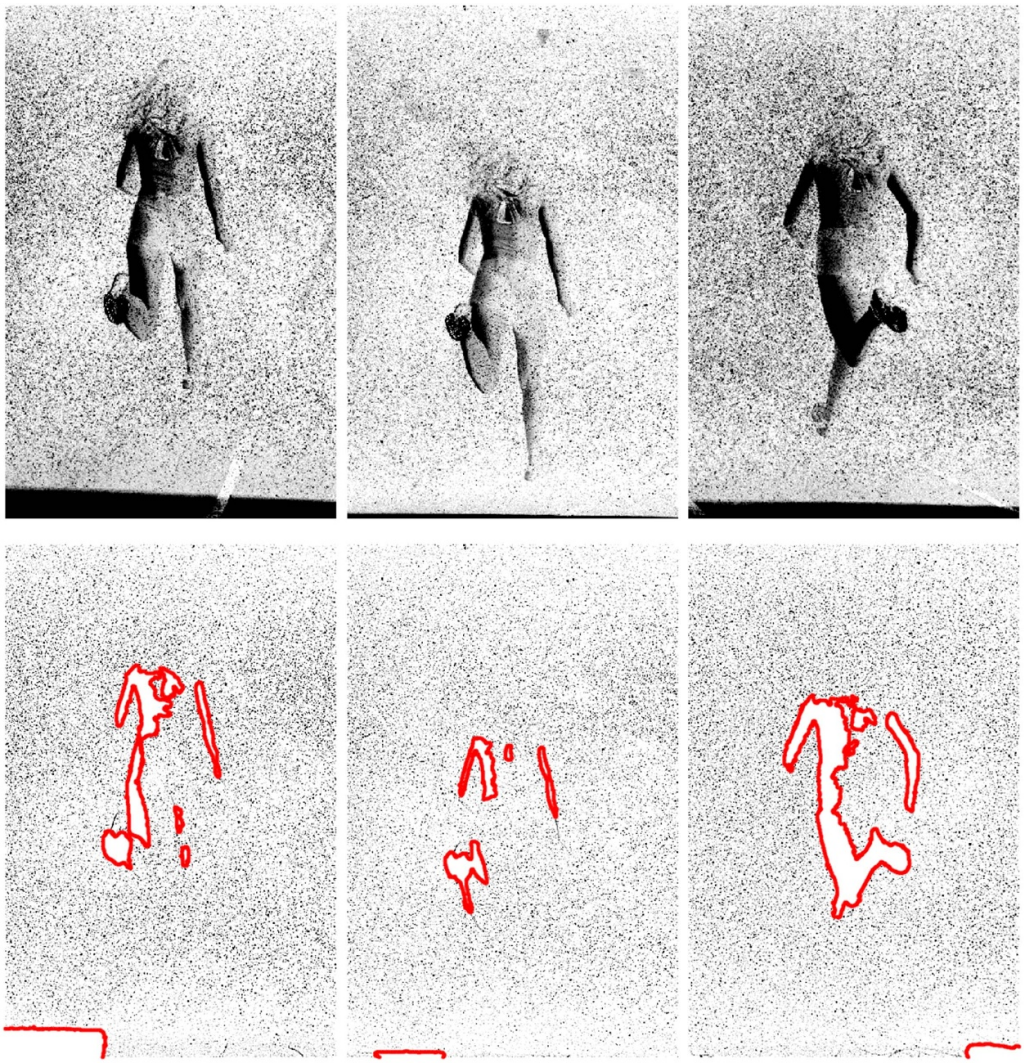

Figure 14. Experimental images of the flow in the near wake of a running athlete. Images from cameras 1(a) to 1(c) (see figure 13) given from left to right. Top: raw images. Bottom: pre-processed images (spatio-temporal high-pass filter), with masked regions indicated in red.

In RoF experiments, slow-moving particles are present away from the measurement target. A time-based high-pass filter applied to the images, as the one discussed in section 2.2, may cancel these out. To avoid it, the normalised frequency of the filter is set to $f = 0$ for the current test case, effectively acting like an average subtraction applied to the sequence. Further using $\kappa = 0.01$ 1/px and the automated masking step returns the image shown in figure 14 (bottom). The current method is able to mask both the stationary reflections (floor) as well as the moving athlete, as indicated in red in the figure.

In the wake of the runner, it can be assumed that the only source of optical blockage is that induced by the light reflections. Without this consideration, it is required that all-three cameras detect a tracer particle, such that $R_{\text{min}} = R_{\text{c}} = 3$. In this scenario, and pre-processing the images without the masking step, particle tracks obtained from the STB algorithm are shown in figure 15 (left). These are coloured by streamwise velocity and represent the trajectories measured in a time interval of eleven snapshots around the frame depicted in figure 14. The residual intensity in the regions of reflections causes the triangulation and tracking of the athlete's foot, which is still travelling through the illuminated domain in the time interval considered here. Apart from that, ghost particles are reconstructed around the silhouette of the runner, mostly on the positive y side since this is the region most severely affected by reflections (see figure 14). These are visible as scattered tracks with unphysically high velocity for their region, and represent approximately 7% of the total number of particles tracked $(N_{\text{g}}/N_{\text{p}} \approx 0.07)$.

The proposed approach is to mask the images, as shown in figure 14 (bottom), and modify the camera coverage rank for every frame independently, such that regions where only two cameras are not blocked ($R_{\text{c}} = 2$) can still be recovered. This approach is more robust than setting $R_{\text{min}} = 2$ everywhere, which would cause the excessive formation of ghost particles due to the low number of viewing directions involved

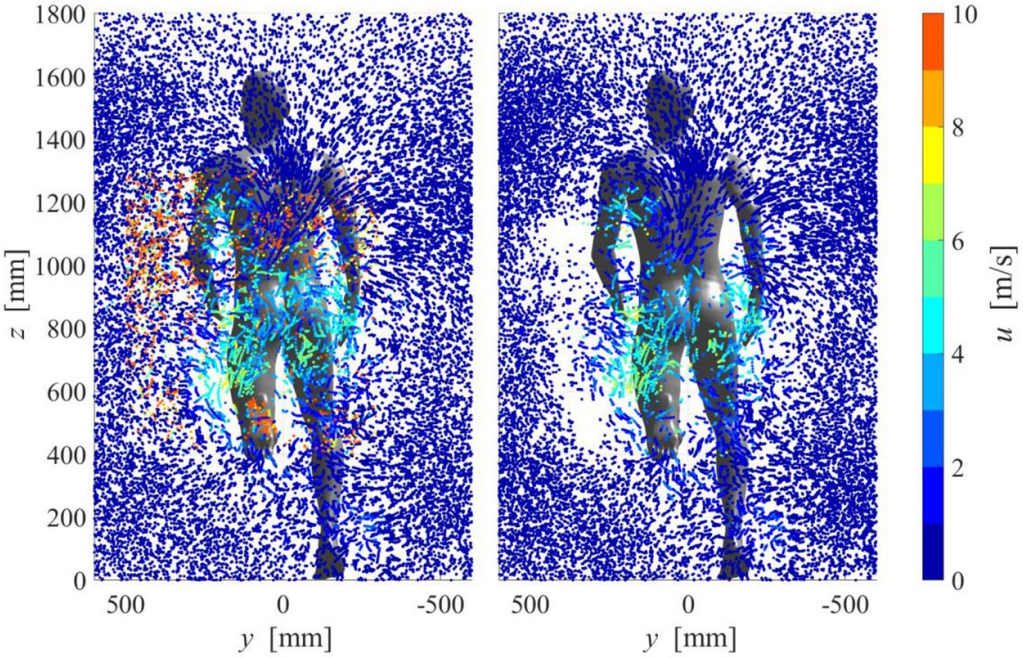

Figure 15. Particle tracks measured in the near wake of a running athlete, from a sequence of 11 snapshots. Left: images have been pre-processed using the spatio-temporal high-pass filter without the masking step. Right: images have been masked and the camera coverage rank has been modified accordingly.

in the triangulation process (Elsinga *et al* 2006). The trajectories obtained by such procedure can be found in figure 15 (right). Ghost particles are not visible in the result, and the regions void of particles (V_{loss}, estimated as those where no particles are reconstructed at double the average inter-particle distance in the domain) are kept to approximately 4% of the DOI.

The resulting flow field reveals a significant streamwise velocity deficit in the near wake, and may be further used for inspection of dominant flow features such as the vortical structures released by the arms and shoulder of the athlete, typically only accessible through numerical simulations (Schickhofer and Hanson 2021).

4. Conclusions

A framework for the treatment of light reflections in volumetric PIV measurements has been introduced. It makes use of the recent development of OA particle tracking strategies (Wieneke and Rockstroh 2024) that account for optical blockage in the measurement volume arising from camera occlusion. Regions of the images affected by light reflections are treated as optically occluded, such that the particle tracking operation is not hampered by the formation of ghost particles (false positives) or data gaps due to cancelled particles (false negatives). The RA-LPT method exploits the concept of camera redundancy to employ the ideal number of cameras in the reconstruction process of every tracer particle.

A masking procedure for volumetric PIV images is introduced as a means of detecting the blinded regions. The method is based on the comparison between the raw image and its high-pass filtered version in the space-time domain, used to generate a mask which, applied to the pre-processed version, creates an image unaffected by reflections. The extracted mask is used to define a region in space not accessible by the affected camera.

Table 3. Ratio of ghost to real particles (N_g/N_p) and volumetric loss (V_{loss}) relative to the two experiments.

	Wall-mounted cube		Running athlete	
	N_g/N_p (%)	V_{loss} (%)	N_g/N_p (%)	V_{loss} (%)
Without masking	35	—	7	—
Only masking	<1	8	<1	20
RA-LPT	<1	0	<1	4

The method has been assessed considering two different experimental conditions, representative of large-scale volumetric PIV applications. First, a wind tunnel experiment is explored, where stationary reflections around the object of interest are formed, adding sources of optical blockage to the camera occlusion problematic. Secondly, a more challenging RoF (Spoelstra *et al* 2019) situation has also been tackled, where the measurement target, a running athlete, creates strong reflections that change significantly in shape and intensity between successive snapshots. In both situations, the method has been shown able of reducing the appearance of ghost particles while maximising the achievable measurement domain, as summarised in table 3.

Data availability statement

The data that support the findings of this study are openly available at the following URL/DOI: https://doi.org/10.4121/6803d03b-d398-4dfe-84e5-762caccb94a6.

Acknowledgments

The experimental images of the sphere and cube have been made available by Constantin Jux and Luuk Hendriksen respectively, who are kindly acknowledged.

The experimental images of the running athlete have been made available by Cristina D'Angelo, Michael Buszek and Wouter Terra, who are kindly acknowledged.

Ethical statement

The experiments were conducted following the guidelines from the TU Delft Human Research Ethics Committee, whereby, prior to the measurements, the participants were informed of the experimental procedures and of the potential risks, and signed a consent form. The research was conducted in accordance with the principles embodied in the Declaration of Helsinki and in accordance with local statutory requirements. No personal data has been shared with people other than the participants; only anonymised data (raw images where the athletes are not recognisable and velocity fields) will be made public.

Author contributions

Adrian Grille Guerra 0009-0006-1136-8988
Conceptualization (equal), Data curation (lead), Methodology (lead), Visualization (lead), Writing – original draft (lead)

Laura Porcar Galan
Conceptualization (equal), Methodology (supporting), Visualization (supporting), Writing – review & editing (supporting)

Andrea Sciacchitano 0000-0003-4627-3787
Conceptualization (equal), Funding acquisition (lead), Supervision (lead), Writing – review & editing (equal)

Fulvio Scarano 0000-0003-2755-6669
Conceptualization (equal), Funding acquisition (lead), Supervision (lead), Writing – review & editing (equal)

References

Adrian R J and Westerweel J 2011 *Particle Image Velocimetry* (Cambridge University Press)

Ashton J and Jones P A 2019 The reliability of using a laser device to assess deceleration ability *Sports* **7** 1–9

Bai K and Katz J 2014 On the refractive index of sodium iodide solutions for index matching in PIV *Exp. Fluids* **55** 1704

Bomphrey R J, Henningsson P, Michaelis D and Hollis D 2012 Tomographic particle image velocimetry of desert locust wakes: instantaneous volumes combine to reveal hidden vortex elements and rapid wake deformation *J. R. Soc. Interface* **9** 3378–86

Bross M, Schanz D, Novara M, Eich F, Schröder A and Kähler C J 2023 Turbulent superstructure statistics in a turbulent boundary layer with pressure gradients *Eur. J. Mech. B* **101** 209–18

D'Angelo C, Buszek M, Terra W and Sciacchitano A 2025 On-site investigation of sprinter aerodynamics *J. Wind Eng. Ind. Aerodyn.* submitted

Depardon S, Lasserre J J, Boueilh J C, Brizzi L E and Borée J 2005 Skin friction pattern analysis using near-wall PIV *Exp. Fluids* **39** 805–18

Elsinga G E, Van Oudheusden B W and Scarano F 2006 Experimental assessment of tomographic-PIV accuracy *13th Int. Symp. on Applications of Laser Techniques to Fluid Mechanics* (*Lisbon, Portugal*, *26-29 June, 2006*) vol 1993 pp 26–29

Elsinga G E, Westerweel J, Scarano F and Novara M 2011 On the velocity of ghost particles and the bias errors in tomographic-PIV *Exp. Fluids* **50** 825–38

Flammang B E, Lauder G V, Troolin D R and Strand T E 2011 Volumetric imaging of fish locomotion *Biol. Lett.* **7** 695–8

Friedhoff B, Roettig F, Wennemar K, Hoyer K, Beslac R, Hesseling C & Beck T 2021 Comparison of stereoscopic particle image velocimetry and volumetric particle tracking velocimetry in the wake of a ducted propeller *Ocean Eng.* **234** 109291

Grille Guerra A, Porcar Galan L, Sciacchitano A and Scarano F 2025 Supporting data for: Treatment of light reflections in 3D PIV systems *4TU.ResearchData* (https://doi.org/10.4121/6803d03b-d398-4dfe-84e5-762caccb94a)

Gui L, Merzkirch W and Shu J-Z 1997 Evaluation of low image density PIV recordings with the MQD method and application to the flow in a liquid bridge *J. Flow Visual Image Process.* **4** 333–43

Hendriksen L A, Grille Guerra A, Sciacchitano A and Scarano F 2025 Omnidirectional particle image velocimetry *Proc. 16th Int. Symp. on Particle Image Velocimetry*

Hendriksen L A, Sciacchitano A and Scarano F 2024 Object registration techniques for 3D particle tracking *Meas. Sci. Technol.* **35** 125202

Huhn F, Schanz D, Manovski P, Gesemann S and Schröder A 2018 Time-resolved large-scale volumetric pressure fields of an impinging jet from dense Lagrangian particle tracking *Exp. Fluids* **59** 1–16

Hysa I, Tuinstra M, Sciacchitano A, Scarano F, van der Meulen M J, Rockstroh T and Roosenboom E W M 2024 A multi-directional redundant 3D-LPT system for ship–flight–deck wind interactions *Exp. Fluids* **65** 1–15

Jux C, Sciacchitano A and Scarano F 2020 Flow pressure evaluation on generic surfaces by robotic volumetric PTV *Meas. Sci. Technol.* **31** 104001

Jux C, Sciacchitano A, Schneiders J F G and Scarano F 2018 Robotic volumetric PIV of a full-scale cyclist *Exp. Fluids* **59** 74

Kähler C J, Scholz U and Ortmanns J 2006 Wall-shear-stress and near-wall turbulence measurements up to single pixel resolution by means of long-distance micro-PIV *Exp. Fluids* **41** 327–41

Masullo A and Theunissen R 2017 Automated mask generation for PIV image analysis based on pixel intensity statistics *Exp. Fluids* **58** 1–11

Mertens C, Costa Fernandez J L, Sodja J, Sciacchitano A and van Oudheusden B W 2023 Nonintrusive experimental aeroelastic analysis of a highly flexible wing *AIAA J.* **61** 3062–77

Novara M, Schanz D and Schröder A 2023 Two-pulse 3D particle tracking with shake-the-box *Exp. Fluids* **64** 1–21

Nutta T, Sciacchitano A and Scarano F 2023 Wand-based calibration technique for 3D LPT *15th Int. Symp. on Particle Image Velocimetry*

Paterna E, Moonen P, Dorer V and Carmeliet J 2013 Mitigation of surface reflection in PIV measurements *Meas. Sci. Technol.* **24** 057003

Porcar Galan L, Grille Guerra A, Sciacchitano A and Scarano F 2024 Light reflections detection and correction for robotic volumetric PIV *Proc. Int. Symp. on the Application of Laser and Imaging Techniques to Fluid Mechanics* vol 21 pp 1–19

Saiz G G, Sciacchitano A and Scarano F 2022 On the closure of collar's triangle by optical diagnostics *Exp. Fluids* **63**

Scarano F, Ghaemi S, Caridi G C A, Bosbach J, Dierksheide U and Sciacchitano A 2015 On the use of helium-filled soap bubbles for large-scale tomographic PIV in wind tunnel experiments *Exp. Fluids* **56** 42

Scarano F, Schneiders J F G, Saiz G G and Sciacchitano A 2022 Dense velocity reconstruction with VIC-based time-segment assimilation *Exp. Fluids* **63** 1–15

Schanz D, Gesemann S and Schröder A 2016 Shake-the-box: Lagrangian particle tracking at high particle image densities *Exp. Fluids* **57**

Schickhofer L and Hanson H 2021 Aerodynamic effects and performance improvements of running in drafting formations *J. Biomech.* **122** 110457

Schneiders J F G, Scarano F, Jux C and Sciacchitano A 2018 Coaxial volumetric velocimetry *Meas. Sci. Technol.* **29** 065201

Schröder A, Geisler R, Elsinga G E, Scarano F and Dierksheide U 2008 Investigation of a turbulent spot and a tripped turbulent boundary layer flow using time-resolved tomographic PIV *Exp. Fluids* **44** 305–16

Schröder A and Schanz D 2023 3D Lagrangian particle tracking in fluid mechanics *Annu. Rev. Fluid Mech.* **55** 511–40

Schröder A, Willert C, Schanz D, Geisler R, Jahn T, Gallas Q and Leclaire B 2020 The flow around a surface mounted cube: a characterization by time-resolved PIV, 3D shake-the-box and LBM simulation *Exp. Fluids* **61** 189

Schröder D, Leweke T and Stumpf E 2023 High-speed volumetric particle tracking measurements of unstable helical vortex pairs *Exp. Fluids* **64** 141

Sciacchitano A and Scarano F 2014 Elimination of PIV light reflections via a temporal high pass filter *Meas. Sci. Technol.* **25** 084009

Spoelstra A, de Martino Norante L, Terra W, Sciacchitano A and Scarano F 2019 On-site cycling drag analysis with the ring of fire *Exp. Fluids* **60** 90

Usherwood J R, Cheney J A, Song J, Windsor S P, Stevenson J P J, Dierksheide U and Bomphrey R J 2020 High aerodynamic lift from the tail reduces drag in gliding raptors *J. Exp. Biol.* **223** jeb214809

Violato D and Scarano F 2011 Three-dimensional evolution of flow structures in transitional circular and chevron jets *Phys. Fluids* **23** 124104

Wang Z, Bovik A C, Sheikh H R and Simoncelli E P 2004 Image quality assessment: from error visibility to structural similarity *IEEE Trans. Image Process.* **13** 600–12

Wieneke B 2008 Volume self-calibration for 3D particle image velocimetry *Exp. Fluids* **45** 549–56

Wieneke B 2013 Iterative reconstruction of volumetric particle distribution *Meas. Sci. Technol.* **24** 024008

Wieneke B and Rockstroh T 2024 Lagrangian particle tracking in the presence of obstructing objects *Meas. Sci. Technol.* **35** 055303

Willert C 1997 Stereoscopic digital particle image velocimetry for application in wind tunnel flows *Meas. Sci. Technol.* **8** 1465–79

Wolf C C, Schanz D, Schwarz C, Heintz A, Bosbach J, Strübing T and Schröder A 2024 Volumetric wake investigation of a free-flying quadcopter using shake-the-box Lagrangian particle tracking *Exp. Fluids* **65** 152